

A Landmark-Based Image Registration Model using a Nonlinear Elasticity Smoother for Mapping Mouse Atlas to Gene Expression Data

Tungyou Lin¹, Carole Le Guyader³, Ivo Dinov²,
Paul Thompson², Arthur Toga², and Luminita Vese¹

UCLA CAM Report 09-51, June 2009

¹ Department of Mathematics, UCLA

² Laboratory of Neuro Imaging, UCLA School of Medicine

³ IRMAR, UMR CNRS 6625, Institut National des Sciences Appliquées de Rennes

Abstract

This paper is devoted to the registration of gene expression data to a neuroanatomical mouse atlas in two dimensions. We use a nonlinear elasticity regularization allowing large and smooth deformations, and overcome the difficulty of minimizing the nonlinear elasticity functional by introducing an additional variable $\mathbf{v} \simeq \nabla \mathbf{u}$, where \mathbf{u} is the displacement. Thus, the nonlinearity in the derivatives of the unknown \mathbf{u} no longer exists in the obtained Euler-Lagrange equation. Experimental results show that gene expression data are mapped to their corresponding mouse atlas by minimizing a standard L^2 dissimilarity measure along with landmark constraints. We also present comparisons with biharmonic regularization to show that the proposed nonlinear elasticity model needs fewer numerical correction such as regriding, renders smaller dissimilarity in landmark distance and intensity maps, and produces larger mutual information.

Keywords: mouse atlas, gene expression, registration, nonlinear elasticity, landmark-based, multi-modal.

1 Introduction

An important task in medical imaging, for clinical studies of disease and for atlas-based identification and segmentation of anatomical structures, is to compare a subject/time variant template image T with an unbiased, reference image R . This is commonly done using image registration. Given a reference R and a template T , defined on image domain Ω , we want to find a smooth, invertible transformation to transform T into an image *similar* to R . For images of the same modality, a well-registered template has geometric features and intensity distribution matched with the reference; for images produced by different mechanism and possessing distinct modalities, the goal of registration is to correlate the images while maintaining the modality of the template. In the case of mapping gene expression data to atlas, we want to match anatomically or geometrically significant points for the template with those corresponding ones for the reference. Preliminary results of this work have been published in conference proceedings [13], [14].

1.1 Prior Related Work

An extensive overview of registration models is given in [18], including parametric model such as landmark-based spline registration, and nonparametric models employing linear diffusion, linear elasticity, biharmonic and fluid regularization. Also, variational methods for regularization of the deformation, by linear elasticity or by diffusion tensor, using mutual information and other information-theoretic approaches, are presented in [8] in a theoretical framework.

For models that deal with larger deformation, we refer to [4] for a well-known large deformation fluid registration method (not in variational form), and to a variational registration for large deformations (LDDMM) [1], [17]. The log-unbiased fluid registration method [26], [25] developed more recently also handles large deformation. Besides fluid models, nonlinear elasticity regularization is implemented using the finite element method in [21] and [20]. Non-linear elasticity principles have also been used with the regularized gradient flow in [7].

As for landmark-based registration methods, we refer to [11], where a consistent landmark and intensity-based registration method is presented using thin-plate spline regularization (or biharmonic regularization). Another related reference is [22] where data fidelity, spline regularization and soft landmark constraints are combined, as in the present work.

1.2 Our Approach

There are forward and backward registrations. The former is done in the Lagrangian framework where a forward transformation Ψ is sought and grid points x with intensity values $T(x)$ are moved and arrive at non-grid points y with intensity values $T(\Psi^{-1}(y)) = T(x)$, $\forall x \in \Omega$ or $\forall y \in \Psi(\Omega)$. In this work, we adopt the Eulerian framework to find a backward transformation $\Phi = \Psi^{-1}$ such that grid points y in the deformed image arrive from non-grid points $x = \Phi(y)$ and are assigned with intensity values $T(x) = T(\Phi(y))$. For more detailed description of the two frameworks, readers may refer to [18].

For data fidelity, we minimize the L^2 distance of the pixel by pixel intensity values between $T \circ \Phi$ and R . The mapping of landmark points is done simply by minimizing the sum of the squared distances between the points without incorporating any spline model. We propose a nonlinear elasticity model for regularization of the displacement vector field, since this allows smooth larger deformations and thus will do without the need for regridding most of the time. In prior work based on nonlinear elasticity principles, the finite element method has been used. To have a simpler numerical algorithm, we hereby introduce an auxiliary variable for the Jacobian matrix of the displacement in order to remove the nonlinearity in the derivatives of the displacement vector field. This idea has been inspired by a more theoretical work [16], and [9] for a joint segmentation and registration model.

1.3 Motivation for Mapping Gene Expression to Atlas

The C57BL/6J mouse digital brain atlas [15], [12] is a comprehensive framework for storing and accessing information, and serves as a canonical representation of the mouse brain. We use the mouse brain atlas as a common and unbiased framework and map gene expression data to the atlas in order to facilitate the integration of anatomic, genetic, and physiologic observations from multiple subjects in a common space. Since genetic mutations and knock-out strains of mice provide critical models for a variety of human diseases, such linkage between genetic information and anatomical structure is important.

2 Description of the Proposed Model

Let Ω be a bounded open subset of \mathbb{R}^d . In present work, we consider two-dimensional images; *i.e.* $d = 2$. Denote by R the reference image and by T the template image. We want to find a smooth transformation $\Phi(\mathbf{x}) = \mathbf{x} + \mathbf{u}(\mathbf{x})$, $\mathbf{x} = (x_1, x_2)$ that minimizes an energy functional consisting of data fidelity, landmark constraints, and regularization. The general form of such functional is as follows,

$$\inf_{\mathbf{u}} \left\{ J(\mathbf{u}) = Fid_{T,R}(\mathbf{u}) + \gamma D^{LM}(\mathbf{u}) + \alpha Reg(\mathbf{u}) \right\},$$

where γ and α are parameters chosen based on the images. By gradient descent, we solve the time-dependent Euler-Lagrange equation in the displacement vector field $\mathbf{u} = (u_1, u_2)$, instead of directly in Φ :

$$\frac{\partial u_l}{\partial t} = -\frac{\partial Fid(\mathbf{u})}{\partial u_l} - \gamma \frac{\partial D^{LM}(\mathbf{u})}{\partial u_l} - \alpha \frac{\partial Reg(\mathbf{u})}{\partial u_l}, \quad l = 1, 2.$$

2.1 Data Fidelity in Eulerian Framework

We have chosen the standard L^2 distance as dissimilarity measure between $T \circ \Phi$ and R , and this is complemented by the use of additional landmarks as geometrical constraints. We minimize the L^2 distance function

$$Fid(\mathbf{u}) = \frac{1}{2} \int_{\Omega} |T(\mathbf{x} + \mathbf{u}(\mathbf{x})) - R(\mathbf{x})|^2 d\mathbf{x}$$

by solving the Euler-Lagrange equation

$$\frac{\partial Fid(\mathbf{u})}{\partial u_l} = (T(\mathbf{x} + \mathbf{u}(\mathbf{x})) - R(\mathbf{x})) T_{x_l}(\mathbf{x} + \mathbf{u}(\mathbf{x})), \quad l = 1, 2$$

where T_{x_l} denotes the gradient of the intensity field of the template in the direction of x_l , $l = 1, 2$.

2.2 Landmark Constraints

Let $\mathbf{x}^{R,k}$ be manually-selected landmark points for the reference R , and $\mathbf{x}^{T,k}$ those for the template T . We want to map $\mathbf{x}^{R,k}$ to $\mathbf{x}^{T,k}$ by a smooth deformation Φ such that $\Phi(\mathbf{x}^{R,k}) \sim \mathbf{x}^{T,k}$ by minimizing the following landmark distance function:

$$D^{LM}(\mathbf{u}) = \frac{1}{2} \sum_{k=1}^m \|\mathbf{x}^{T,k} - \Phi(\mathbf{x}^{R,k})\|^2$$

where $\Phi(\mathbf{x}^{R,k}) = \mathbf{x}^{R,k} + \mathbf{u}(\mathbf{x}^{R,k})$. Then, we solve the following time-dependent Euler-Lagrange equation by gradient descent: $\frac{\partial D^{LM}(\mathbf{u})}{\partial t}(\mathbf{x}) = \begin{cases} \mathbf{x}^{T,k} - \mathbf{x} - \mathbf{u}(\mathbf{x}) & \text{if } \mathbf{x} = \mathbf{x}^{R,k} \\ 0 & \text{otherwise} \end{cases}$, $k = 1, \dots, m$. ($m = \text{number of landmarks}$)

2.3 Regularization

Viewing the shape change of the image after transformation as the deformation of an elastic material under external force was first adopted by [2] in developing linear elastic registration method. Since the linear model works better for small deformation, we propose a nonlinear elastic model to allow large deformation. Among the various nonlinear elastic models, we have chosen the St. Venant-Kirchhoff material for its simplicity [5].

Compared with the experimental results on characteristic images by models with linear diffusion, linear elasticity and biharmonic regularization, the proposed nonlinear elasticity model allows larger and smoother deformation without numerical correction such as regriding [4] most of the time. Since the nonlinear term has resulted in an Euler-Lagrange equation which is hard for numerical implementation, we propose a particular implementation that removes the non-linearity in the derivatives [16], [9].

2.3.1 Diffusion Regularization

Diffusion regularization defined as follows:

$$Reg(\mathbf{u}) = \frac{1}{2} \sum_{l=1}^2 \int_{\Omega} \|\nabla u_l\|^2 d\mathbf{x}$$

is motivated by its smoothing properties and also by its small number of operations required [18]. Solving the Euler-Lagrange equations by gradient descent:

$$\frac{\partial u_l}{\partial t} = -(T(\mathbf{x} + \mathbf{u}(\mathbf{x})) - R(\mathbf{x}))T_{x_l}(\mathbf{x} + \mathbf{u}(\mathbf{x})) + \gamma \frac{\partial D^{LM}(\mathbf{u})}{\partial t}(\mathbf{x}) + \alpha \Delta u_l, \quad l = 1, 2.$$

Each component of the displacement \mathbf{u} is the solution of the heat equation. In the present work, we discretize the time-dependent Euler-Lagrange equations by the following semi-implicit finite difference scheme:

$$\begin{aligned} \frac{u_{l,i,j}^{n+1} - u_{l,i,j}^n}{\Delta t} &= -\left(\frac{\partial T_1}{\partial x_l}\right)_{i,j} (T_{i,j} - R_{i,j}) + \gamma \frac{\partial D^{LM}(\mathbf{u})}{\partial t}(\mathbf{x}) \\ &+ \alpha \left(\frac{u_{l,i+1,j}^n - 2u_{l,i,j}^{n+1} + u_{l,i-1,j}^n}{h^2} + \frac{u_{l,i,j+1}^n - 2u_{l,i,j}^{n+1} + u_{l,i,j-1}^n}{h^2} \right), \quad l = 1, 2, \end{aligned}$$

where $\frac{\partial T_1}{\partial x_l}$ has values on the grid points and is obtained by applying Matlab interpolation function to the gradient T_{x_l} .

2.3.2 Biharmonic Regularization

The biharmonic regularization is defined as

$$Reg(\mathbf{u}) = \frac{1}{2} \sum_{l=1}^2 \int_{\Omega} (\Delta u_l)^2 d\mathbf{x}.$$

The integrand $(\Delta u_l)^2$ approximates the curvature and thus this regularizer minimizes the curvature of the displacement vectors [18]. According to [18], among the nonlinear methods,

the biharmonic registration is less dependent on the initial position of the image and thus is more suitable when an affine linear pre-registration is not available. The time-dependent Euler-Lagrange equations are the following:

$$\frac{\partial \mathbf{u}}{\partial t} = -(T(\mathbf{x} + \mathbf{u}(\mathbf{x})) - R(\mathbf{x}))T_{x_l}(\mathbf{x} + \mathbf{u}(\mathbf{x})) + \gamma \frac{\partial D^{LM}(\mathbf{u})}{\partial t}(\mathbf{x}) - \alpha \Delta^2 \mathbf{u}, \quad l = 1, 2.$$

The semi-implicit finite difference scheme that we adopted is as follows:

$$\begin{aligned} \frac{u_{i,j}^{n+1} - u_{i,j}^n}{\Delta t} &= -\left(\frac{\partial T_1}{\partial x_l}\right)_{i,j} (T_{i,j} - R_{i,j}) + \gamma \frac{\partial D^{LM}(\mathbf{u})}{\partial t}(\mathbf{x}) - \alpha \frac{1}{h^4} (16u_{i,j}^{n+1} \\ &+ u_{i+2,j}^n - 6u_{i+1,j}^n - 6u_{i-1,j}^n + u_{i-2,j}^n + u_{i,j+2}^n - 6u_{i,j+1}^n - 6u_{i,j-1}^n + u_{i,j-2}^n \\ &+ u_{i+1,j+1}^n + u_{i+1,j-1}^n + u_{i-1,j+1}^n + u_{i-1,j-1}^n), \quad l = 1, 2. \end{aligned}$$

2.3.3 Linear and Nonlinear Elasticity Regularization

It is physically motivated to view the displacement of vector fields as the deformation of some material under force. The strain energy corresponding to Saint Venant-Kirchhoff hyperelastic materials [24] is given by

$$Reg(\mathbf{u}) = \int_{\Omega} W(\epsilon) d\mathbf{x},$$

with tensor

$$\epsilon(\mathbf{u}) = \frac{1}{2}(\nabla \mathbf{u}^t + \nabla \mathbf{u} + \nabla \mathbf{u}^t \nabla \mathbf{u}).$$

and the stored energy

$$W(\epsilon) = \frac{\lambda}{2}(\text{trace}(\epsilon))^2 + \mu \text{trace}(\epsilon^2),$$

where λ and μ are the Lamé coefficients of the material.

Linear Elasticity Regularization By removing the nonlinear term $\nabla \mathbf{u}^t \nabla \mathbf{u}$, we obtain the linear elasticity regularization which allows small deformation. The time-dependent Euler-Lagrange equations are as follows:

$$\frac{\partial \mathbf{u}}{\partial t} = -(T(\mathbf{x} + \mathbf{u}(\mathbf{x})) - R(\mathbf{x}))T_{x_l}(\mathbf{x} + \mathbf{u}(\mathbf{x})) + \gamma \frac{\partial D^{LM}(\mathbf{u})}{\partial t}(\mathbf{x}) + \alpha \mu \Delta \mathbf{u} + (\lambda + \mu) \nabla(\text{div} \mathbf{u}), \quad l = 1, 2.$$

The semi-implicit finite difference scheme for the regularization term is the following:

$$\begin{aligned} \frac{u_{p,i,j}^{n+1} - u_{p,i,j}^n}{\Delta t} &= -\left(\frac{\partial T_1}{\partial x_l}\right)_{i,j} (T_{i,j} - R_{i,j}) + \gamma \frac{\partial D^{LM}(\mathbf{u})}{\partial t}(\mathbf{x}) \\ &+ (\lambda + \mu) A_p + \mu \left(\frac{u_{p,i+1,j}^n - 2u_{p,i,j}^{n+1} + u_{p,i-1,j}^n}{h^2} + \frac{u_{p,i,j+1}^n - 2u_{p,i,j}^{n+1} + u_{p,i,j-1}^n}{h^2} \right) \\ &+ (\lambda + \mu) \left(\frac{u_{q,i+1,j+1}^n - u_{q,i+1,j-1}^n - u_{q,i-1,j+1}^n + u_{q,i-1,j-1}^n}{4h^2} \right), \end{aligned}$$

where $p, q = 1, 2, p \neq q$, $A_1 = \frac{u_{2,i+1,j}^n - 2u_{2,i,j}^{n+1} + u_{2,i-1,j}^n}{h^2}$, $A_2 = \frac{u_{2,i,j+1}^n - 2u_{2,i,j}^{n+1} + u_{2,i,j-1}^n}{h^2}$

Nonlinear Elasticity Regularization To allow larger deformation, we keep the nonlinear term and the regularization is as follows:

$$\begin{aligned} Reg(\mathbf{u}) &= \frac{\lambda}{8} \left(2(\operatorname{div} \mathbf{u}) + \sum_{k=1}^2 |\nabla u_k|^2 \right)^2 \\ &+ \frac{\mu}{4} \left(\sum_{i=1}^2 \left[2 \frac{\partial u_i}{\partial x_i} + \sum_{k=1}^2 \left(\frac{\partial u_k}{\partial x_i} \right)^2 \right]^2 + \sum_{i,j=1, i \neq j}^2 \left[\frac{\partial u_j}{\partial x_i} + \frac{\partial u_i}{\partial x_j} + \sum_{k=1}^2 \frac{\partial u_k}{\partial x_i} \frac{\partial u_k}{\partial x_j} \right]^2 \right). \end{aligned}$$

It is cumbersome to directly compute and discretize the associated Euler-Lagrange equation in \mathbf{u} . To avoid this difficulty, we introduce a matrix variable $\mathbf{v} = \begin{pmatrix} v_{11} & v_{12} \\ v_{21} & v_{22} \end{pmatrix}$, which approximates $\nabla \mathbf{u}$. For β large enough, $Reg(\mathbf{u})$ can be well approximated by

$$\begin{aligned} Reg_\beta(\mathbf{u}, \mathbf{v}) &= \int_{\Omega} \left[W \left(\frac{1}{2} (\mathbf{v}^t + \mathbf{v} + \mathbf{v}^t \mathbf{v}) \right) + \beta |\mathbf{v} - \nabla \mathbf{u}|^2 \right] dx \\ &= \int_{\Omega} \left(\frac{\lambda}{8} [2(v_{11} + v_{22}) + (v_{11}^2 + v_{12}^2 + v_{21}^2 + v_{22}^2)]^2 \right. \\ &+ \frac{\mu}{4} [(2v_{11} + v_{11}^2 + v_{21}^2)^2 + (2v_{22} + v_{12}^2 + v_{22}^2)^2 + 2(v_{12} + v_{21} + v_{11}v_{12} + v_{21}v_{22})^2] \left. \right) dx \\ &+ \beta \int_{\Omega} \left[\left| v_{11} - \frac{\partial u_1}{\partial x_1} \right|^2 + \left| v_{12} - \frac{\partial u_1}{\partial x_2} \right|^2 + \left| v_{21} - \frac{\partial u_2}{\partial x_1} \right|^2 + \left| v_{22} - \frac{\partial u_2}{\partial x_2} \right|^2 \right] dx. \end{aligned}$$

Now, we solve by gradient descent the linearized Euler-Lagrange equations in u_l , $l = 1, 2$:

$$\frac{\partial u_l}{\partial t} = -(T(\mathbf{x} + \mathbf{u}(\mathbf{x})) - R(\mathbf{x})) T_{x_l}(\mathbf{x} + \mathbf{u}(\mathbf{x})) + \gamma \frac{\partial D^{LM}(\mathbf{u})}{\partial t}(\mathbf{x}) + 2\alpha\beta \left(\Delta u_l - \frac{\partial v_{l1}}{\partial x_1} - \frac{\partial v_{l2}}{\partial x_2} \right), \quad l = 1, 2,$$

and then update the approximation matrix \mathbf{v} by solving the four Euler-Lagrange equations in \mathbf{v} :

$$\begin{aligned} \frac{\partial v_{11}}{\partial t} &= 2\alpha\beta \left(\frac{\partial u_1}{\partial x_1} - v_{11} \right) - \alpha\lambda I(1 + v_{11}) \\ &- \alpha\mu(2v_{11} + v_{11}^2 + v_{21}^2)(1 + v_{11}) - \alpha\mu J v_{12}, \\ \frac{\partial v_{12}}{\partial t} &= 2\alpha\beta \left(\frac{\partial u_1}{\partial x_2} - v_{12} \right) - \alpha\lambda I v_{12} \\ &- \alpha\mu(2v_{22} + v_{12}^2 + v_{22}^2)v_{12} - \alpha\mu J(1 + v_{11}), \\ \frac{\partial v_{21}}{\partial t} &= 2\alpha\beta \left(\frac{\partial u_2}{\partial x_1} - v_{21} \right) - \alpha\lambda I v_{21} \\ &- \alpha\mu(2v_{11} + v_{11}^2 + v_{21}^2)v_{21} - \alpha\mu J(1 + v_{22}), \\ \frac{\partial v_{22}}{\partial t} &= 2\alpha\beta \left(\frac{\partial u_2}{\partial x_2} - v_{22} \right) - \alpha\lambda I(1 + v_{22}) \\ &- \alpha\mu(2v_{22} + v_{12}^2 + v_{22}^2)(1 + v_{22}) - \alpha\mu J v_{21}, \end{aligned}$$

where $I = v_{11} + v_{22} + \frac{1}{2}v_{11}^2 + \frac{1}{2}v_{21}^2 + \frac{1}{2}v_{12}^2 + \frac{1}{2}v_{22}^2$, and $J = v_{12} + v_{21} + v_{11}v_{12} + v_{21}v_{22}$. The following are the semi-implicit finite difference schemes for the time-dependent Euler-Lagrange

equations for the regularization term in \mathbf{u} and in \mathbf{v} :

$$\begin{aligned} \frac{u_{i,j}^{n+1} - u_{i,j}^n}{\Delta t} &= -\left(\frac{\partial T_1}{\partial x_l}\right)_{i,j} (T_{i,j} - R_{i,j}) + \gamma \frac{\partial D^{LM}(\mathbf{u})}{\partial t}(\mathbf{x}) \\ &+ 2\alpha\beta \left(\frac{u_{i+1,j}^n - 2u_{i,j}^{n+1} + u_{i-1,j}^n}{h^2} + \frac{u_{i,j+1}^n - 2u_{i,j}^{n+1} + u_{i,j-1}^n}{h^2} \right. \\ &\left. - \frac{v_{l1_{i+1,j}}^n - v_{l1_{i-1,j}}^n + v_{l2_{i,j+1}}^n - v_{l2_{i,j-1}}^n}{2h} \right), \end{aligned}$$

and

$$\begin{aligned} \frac{v_{11}^{n+1} - v_{11}^n}{\Delta t} &= 2\beta \left(\frac{\partial u_1^n}{\partial x_1} - v_{11}^{n+1} \right) - (\lambda E_1 E_5 + \mu(E_2 E_5 + E_3 v_{12})), \\ \frac{v_{12}^{n+1} - v_{12}^n}{\Delta t} &= 2\beta \left(\frac{\partial u_1^n}{\partial x_2} - v_{12}^{n+1} \right) - (\lambda E_1 v_{12} + \mu(E_4 v_{12} + E_3 E_5)), \\ \frac{v_{21}^{n+1} - v_{21}^n}{\Delta t} &= 2\beta \left(\frac{\partial u_2^n}{\partial x_1} - v_{21}^{n+1} \right) - (\lambda E_1 v_{21} + \mu(E_2 v_{21} + E_3 E_6)), \\ \frac{v_{22}^{n+1} - v_{22}^n}{\Delta t} &= 2\beta \left(\frac{\partial u_2^n}{\partial x_2} - v_{22}^{n+1} \right) - (\lambda E_1 E_6 + \mu(E_4 E_6 + E_3 v_{21})), \end{aligned}$$

where

$$\begin{aligned} E_1 &= v_{11} + \frac{1}{2}v_{11}^2 + \frac{1}{2}v_{21}^2 + v_{22} + \frac{1}{2}v_{12}^2 + \frac{1}{2}v_{22}^2, \\ E_2 &= 2v_{11} + v_{11}^2 + v_{21}^2, E_3 = 2v_{22} + v_{12}^2 + v_{22}^2, \\ E_4 &= v_{12} + v_{21} + v_{11}v_{12} + v_{21}v_{22}, E_5 = 1 + v_{11}, E_6 = 1 + v_{22}. \end{aligned}$$

3 Experimental Results

3.1 Numerical Correction: Regridding

An admissible deformation field $\Phi : \bar{\Omega} \rightarrow \bar{\Omega}$, $\Phi(\mathbf{x}) = \mathbf{x} + \mathbf{u}(\mathbf{x})$, should satisfy $\det(\nabla\Phi) > 0$ in Ω , $\Phi(\mathbf{x}) = \mathbf{x}$ on $\partial\Omega$, and Φ is one-to-one and onto on $\bar{\Omega}$. To enforce such a constraint, some numerical corrections such as regridding are introduced [4]. In present work, if $\det(\nabla(\Phi)^{n+1}) < 0.025$, we set the displacement field $\mathbf{u}^{n+1} = \mathbf{0}$, the template $T(\mathbf{x}) = T(\mathbf{x} + \mathbf{u}^n)$, and the landmarks, if any, $\mathbf{x}^{R,k} = \mathbf{x}^{T,k} - \mathbf{u}^n(\mathbf{x}^{R,k})$. After the iteration is done, we calculate the composite displacement field by interpolating each of the intermediate displacement field, which are saved during the regridding process, based on its succeeding one. The algorithm is given as follows:

- (1) formulate identity matrices S_1 and S_2 so that $S_1(x, y) = x$, $S_2(x, y) = y$;
initialize $\mathbf{u}^n = (u_1^n, u_2^n)$;
- (2) iteration starts: compute \mathbf{u}^{n+1} ;
update matrices S_{11} and S_{22} so that $S_{11}^{n+1} = S_1 + u_1^{n+1}$, $S_{22}^{n+1} = S_2 + u_2^{n+1}$;
if $\det(\text{Jacobian}(\Phi)) < \text{tol}$,
then $\text{regrid.count} = \text{regrid.count} + 1$;
 $T = T_1$;
 $\mathbf{u}^{n+1} = \mathbf{0}$;
save \mathbf{u}^n as data files $u_k(\text{regrid.count})$, $k = 1, 2$;

```

end;
(3) iteration ends:
if regrid.count > 0
then composite. $S_{kk} = S_{kk}^{final.iteration}$ ;
composite. $u_k = u_k^{final.iteration}$ ,  $k = 1, 2$ ;
for  $i = regrid.count : -1 : 1$ 
read and load data files  $u_k(regrid.count)$ ;
 $U0_k = u_k(regrid.count)$ ,  $k = 1, 2$ ;
composite. $u_k(regrid.count) = composite.u_k(regrid.count)$ 
+interpolation( $U0_k, composite.S_{22}, composite.S_{11}$ );
composite. $S_{kk}(regrid.count) = S_k + composite.u_k(regrid.count)$ ;
end
 $u_k = composite.u_k(1)$ ;
 $S_{kk} = composite.S_{kk}$ .

```

Note that models requiring fewer regridding steps are considered better since a well-defined transformation is desired. The following results are done mostly without regridding.

3.2 Synthetic Images

3.2.1 Disk to Letter C

We first compare the linear elasticity, linear diffusion, biharmonic, and nonlinear elasticity models for registration from disk to letter C (Figure 1.)



Figure 1: Reference (left), Template (right).

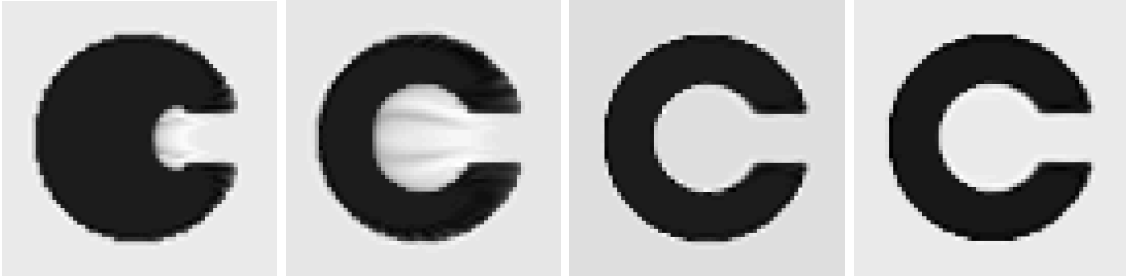


Figure 2: (left to right) Transformed Images by linear elasticity, linear diffusion, biharmonic (BH), nonlinear elasticity (NE).

From the registration results (Figure 2), we can see that linear elasticity regularization is only suitable for small deformation. The linear diffusion regularization works better but introduces a lot of artifacts. The biharmonic model seems to render a more satisfactory result (even though a darker background is observed) together with the nonlinear elasticity model. In terms of the regridding numbers, the biharmonic model and the nonlinear elasticity model require three regridding steps while the linear diffusion model requires four.

3.2.2 Other Binary Images

We further compare the four models for registration of other binary images (Figure 3.) We found from the registration results (Figure 4) that the nonlinear elasticity model does not introduce artifacts (*e.g.* under the right ear where we expect the largest deformation) like other models do. In terms of regridding numbers, the nonlinear elasticity model is the only one which does not require any regridding step, and the biharmonic model requires fewer regridding steps than the other two linear models.



Figure 3: Reference (left), Template (right).

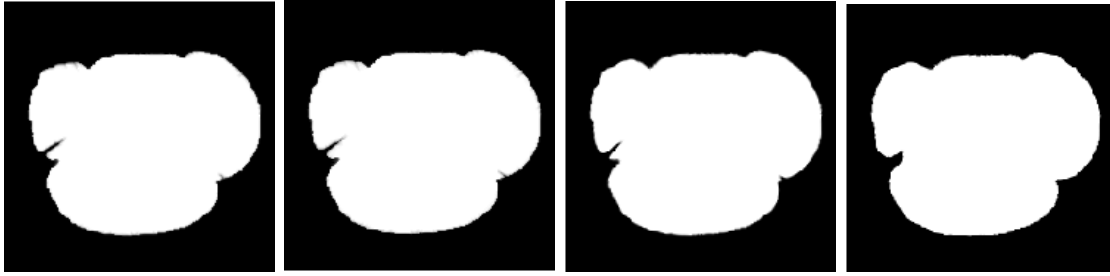


Figure 4: (left to right) Transformed Images by linear elasticity, linear diffusion, biharmonic (BH), nonlinear elasticity (NE).

Since the biharmonic model is more comparable to the nonlinear elasticity model, we want to further examine the two models for some real data.

3.3 Real Data

3.3.1 Ground Truth Test

Given two MRI images R and T (Figure 5) and the true distortion map (Figure 6) from R to T (data test kindly provided by H. Tagare [23]), we want to check if the distortion maps rendered by the nonlinear elasticity model and the biharmonic model are similar to the true map. The true distortion map plots the vector fields from R to T , and the dissimilarity between the true map and the maps after registration by the two models is measured by the Euclidean vectorial norm. The difference from the ground truth is slightly smaller for the nonlinear elasticity model after the same number of iterations (Figure 7.)

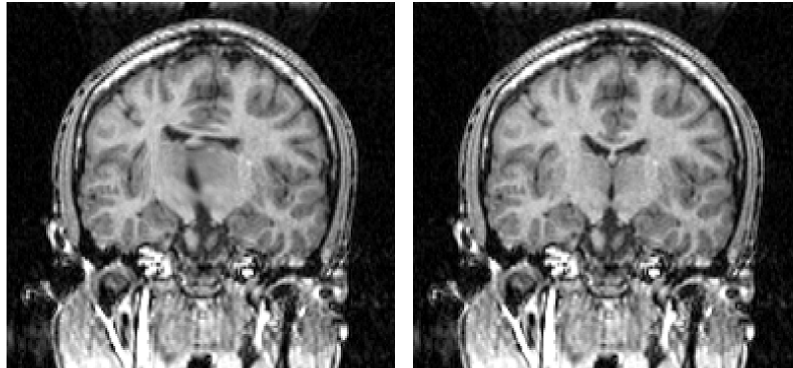


Figure 5: Reference (left), Template (right).

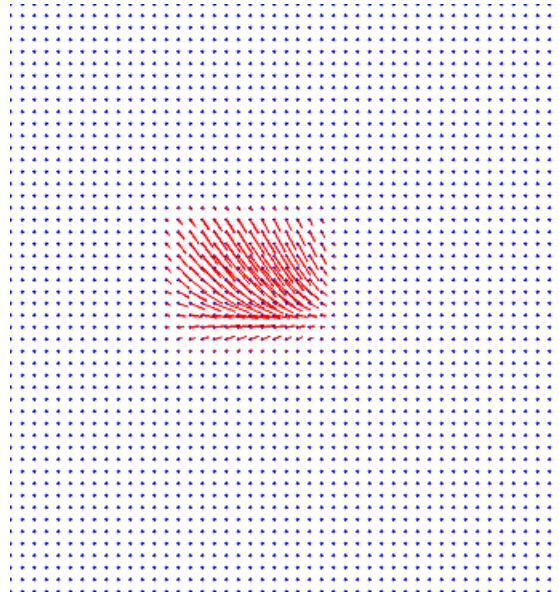


Figure 6: True Map.

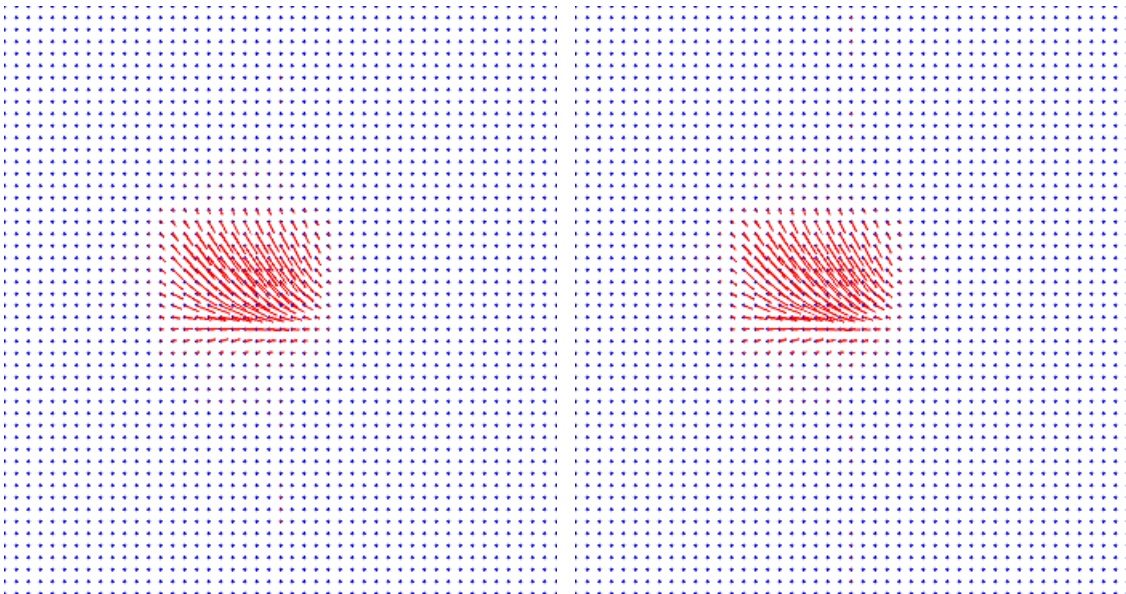


Figure 7: Distortion maps by BH (left), NE (right); Difference from the ground truth is 0.12692 for BH model and 0.12413 for NE model.

3.3.2 Gene Expression to Atlas

We now show some experimental results obtained by the two methods presented in the previous section for mapping one 2D slice of mouse brain gene expression data (template T) to its corresponding 2D slice of the mouse brain atlas (reference R), in the presence of landmarks. The data is provided by the Center for Computational Biology, UCLA. The mouse atlas acquired from the LONI database was pre-segmented. The gene expression data was segmented manually to facilitate data processing in other applications. Some studies have developed algorithms for automatically segmenting the brain area of gene expression data. Moreover, since the intensity range and intensity values of the gene expression data are so small that the images almost resemble to characteristic images, we also match the histogram of the gene expression data to that of the atlas in order to facilitate better registration for area away from the edges. The two models have been independently tested on 8 pairs, all of size 200x200 pixels. The non-brain regions have been removed, to produce better matching. The number of iterations for both methods depends on how small we wish the landmark distance and the similarity measure to be. The landmarks are marked by an experienced neuroanatomist based on the anatomical structures present in the images. This is based on prior knowledge in neuroanatomy.

Energy Fig.8 shows the energy decreasing with time for both models applied on Pair 5.

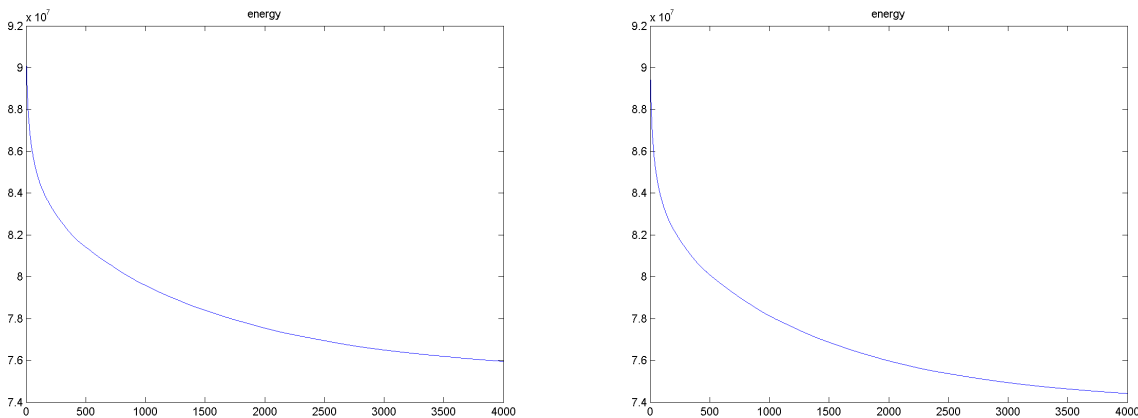


Figure 8: Energy decreasing with time using BH (left) and NE (right) model.

Landmark Convergence Fig.9 shows the landmark convergence with and without the enforcement of landmark constraints. We see that the convergence is much faster with the enforcement of the constraints.

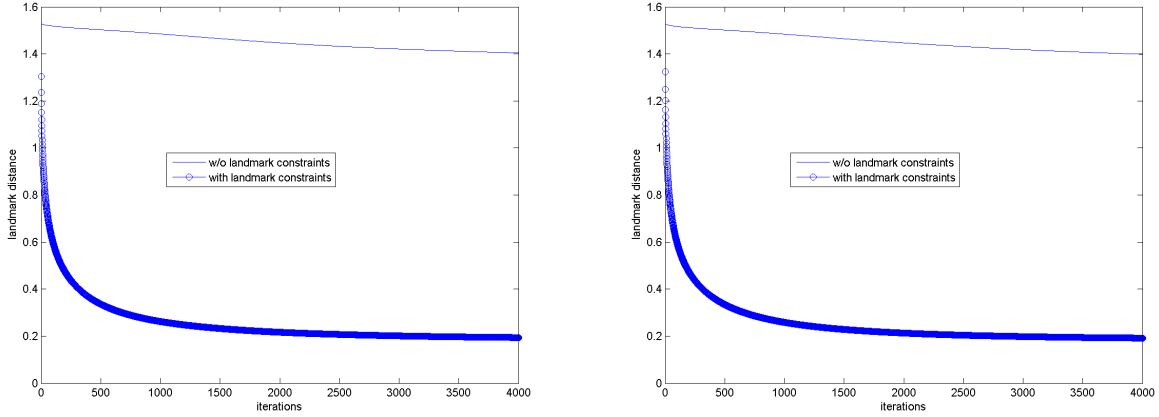


Figure 9: Landmarks converging with time using BH (left) and NE (right) model. Top/bottom line for convergence without/with enforcement of landmark constraints.

Visualization of Registration Results Fig.10 to Fig.17 are registration results of the eight pairs of images after the same number of iterations for both models. Each figure contains (1) a reference-template (before and after histogram equalization) data pair with landmark points marked, (2) the deformed template, distortion map with landmark points marked, and (3) inverse of the determinant of Jacobian of Φ with deformed grid. The distortion maps draw the vectors from the grid points of the reference image to the non-grid points after registration; the original reference/template landmarks are marked in red/green, the reference landmarks after registration are marked in blue. We can see that the landmarks converge (moving from red spots to blue spots to approach the green spots) in accordance with the distortion field. As for the deformed grids, where the grid area expands/shrinks, we observe lighter/darker gray level corresponding to larger/smaller value of the inverse of determinant of Jacobian.

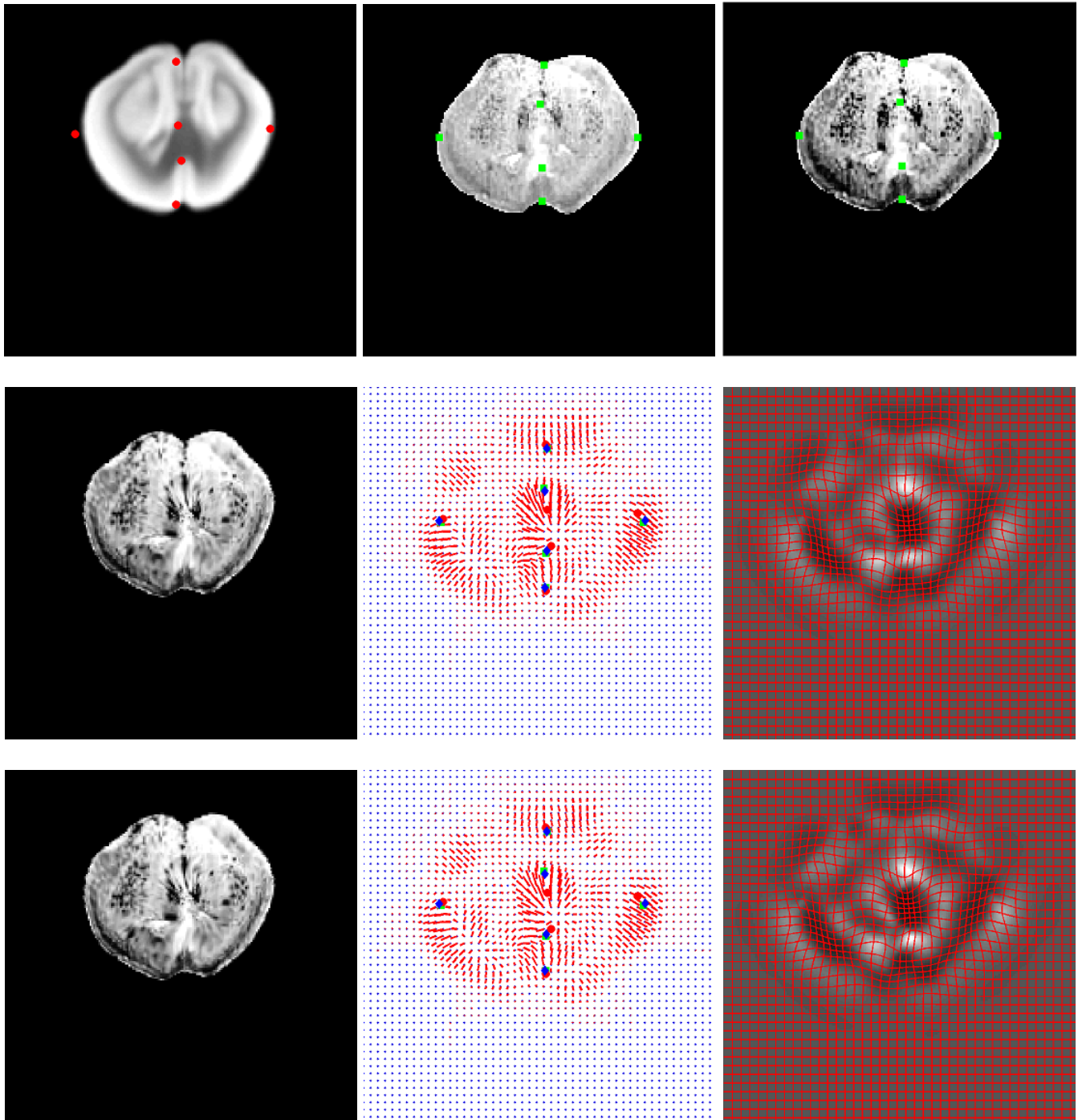


Figure 10: Pair 4: mouse atlas (reference R), gene expression (template T), and gene expression after histogram equalization with specified landmarks (top from left to right); deformed template, deformation field plus the landmarks transformation, $1/\det(\nabla\Phi)$ plus the deformed grid using BH regularization (middle from left to right), and those using NE regularization (bottom from left to right.)

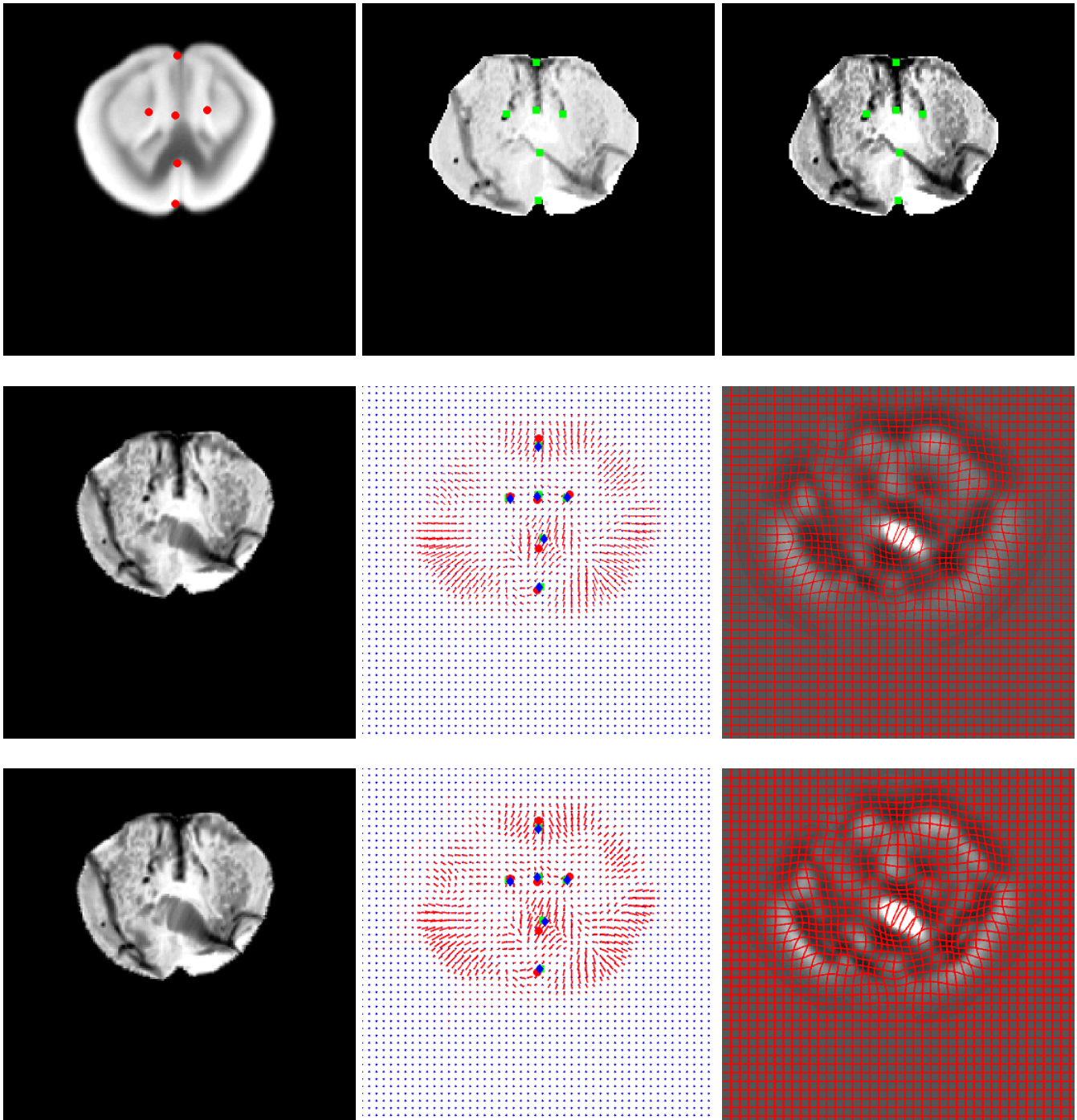


Figure 11: Pair 5: mouse atlas (reference R), gene expression (template T), and gene expression after histogram equalization with specified landmarks (top from left to right); deformed template, deformation field plus the landmarks transformation, $1/\det(\nabla\Phi)$ plus the deformed grid using BH regularization (middle from left to right), and those using NE regularization (bottom from left to right.)

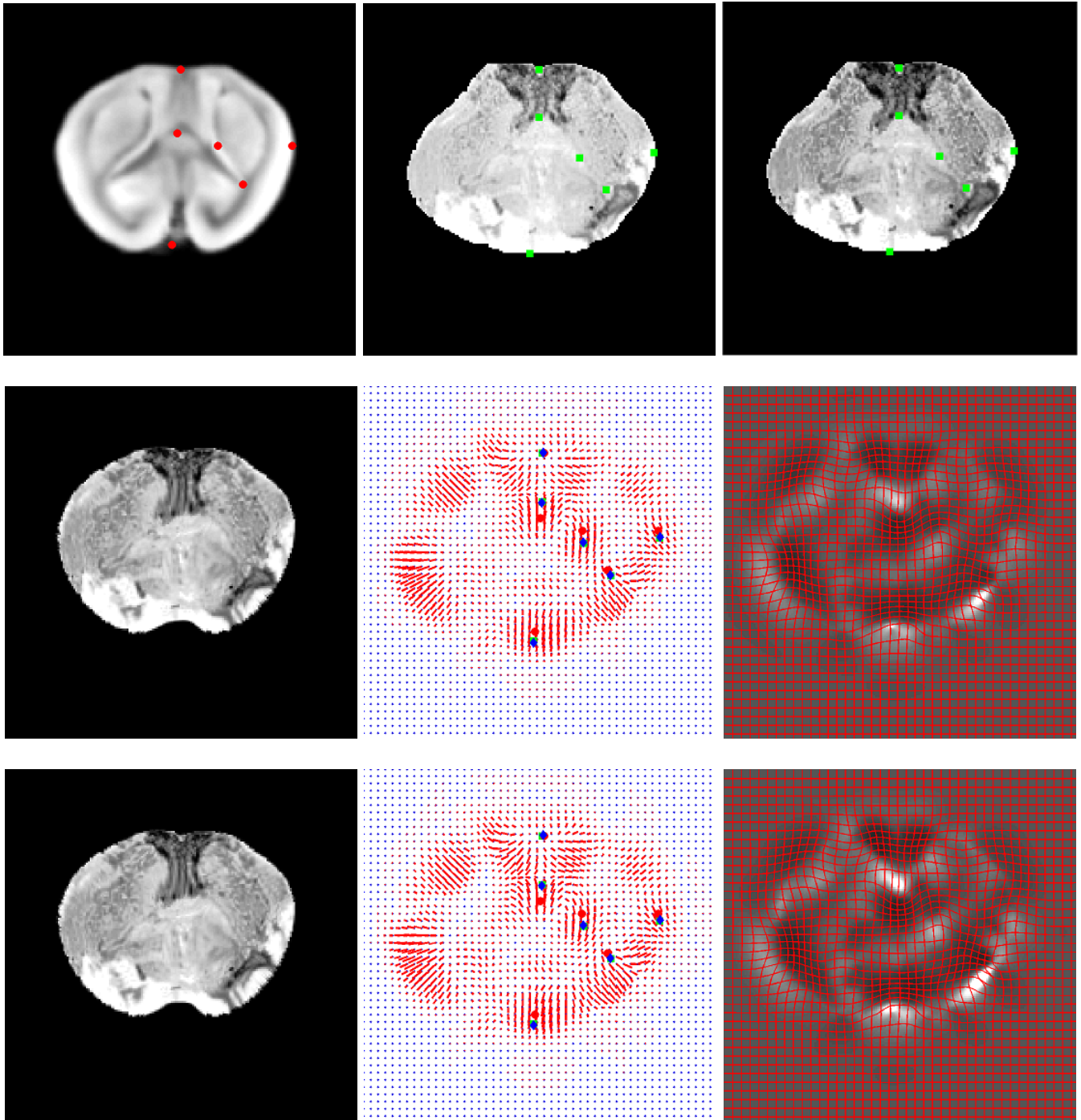


Figure 12: Pair 6: mouse atlas (reference R), gene expression (template T), and gene expression after histogram equalization with specified landmarks (top from left to right); deformed template, deformation field plus the landmarks transformation, $1/\det(\nabla\Phi)$ plus the deformed grid using BH regularization (middle from left to right), and those using NE regularization (bottom from left to right.)

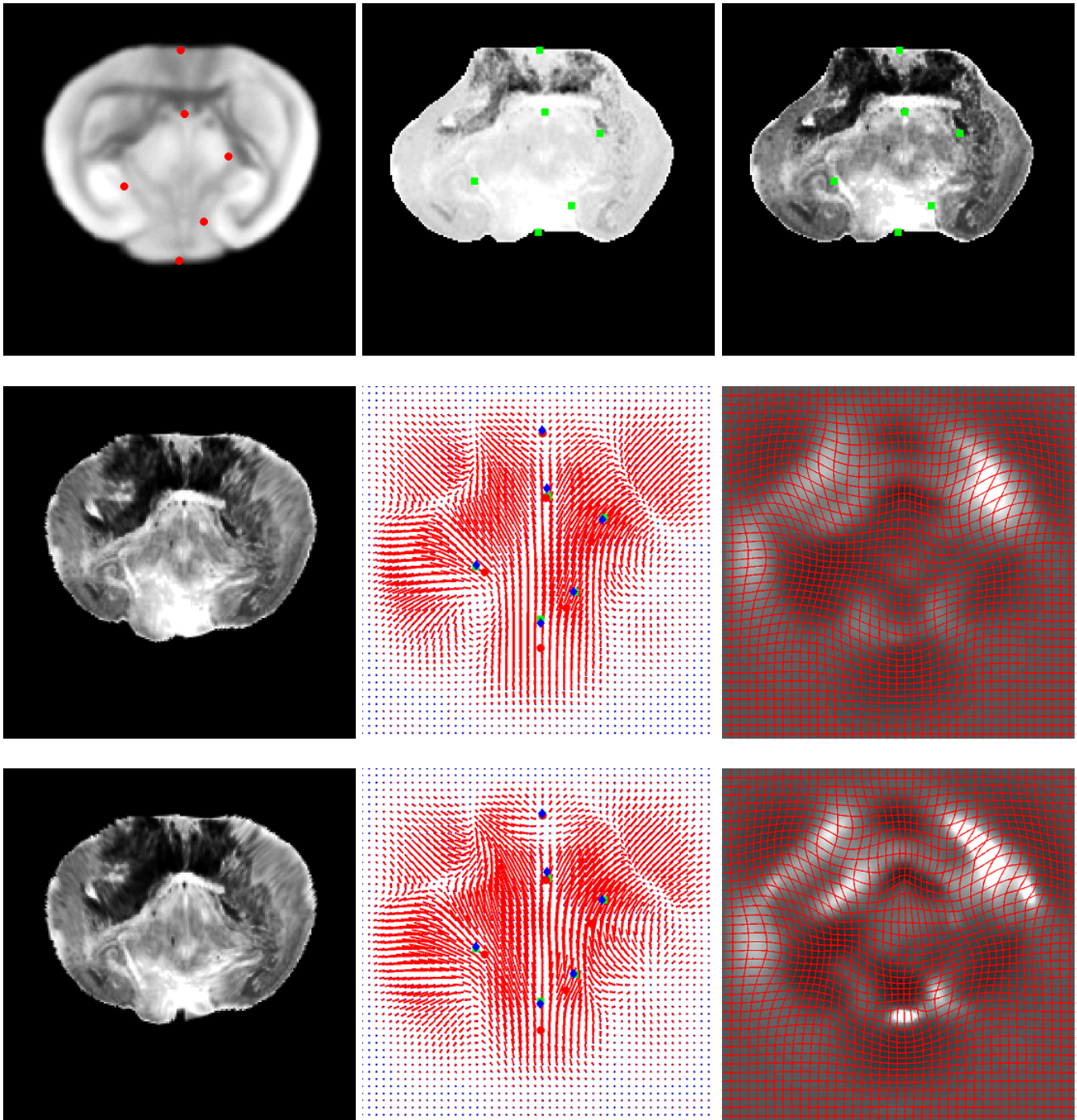


Figure 13: Pair 7: mouse atlas (reference R), gene expression (template T), and gene expression after histogram equalization with specified landmarks (top from left to right); deformed template, deformation field plus the landmarks transformation, $1/\det(\nabla\Phi)$ plus the deformed grid using BH regularization (middle from left to right), and those using NE regularization (bottom from left to right.)

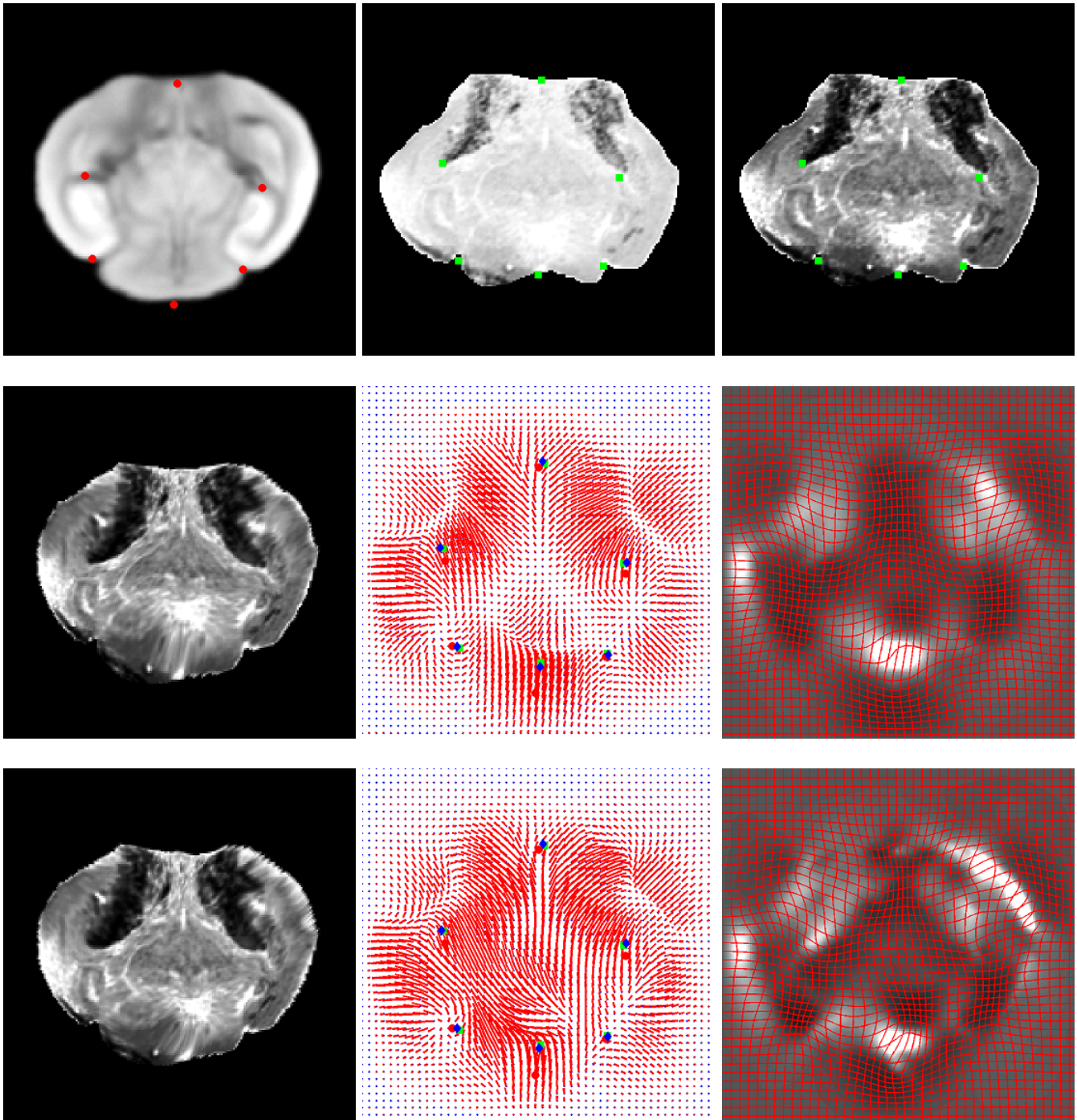


Figure 14: Pair 8: mouse atlas (reference R), gene expression (template T), and gene expression after histogram equalization with specified landmarks (top from left to right); deformed template, deformation field plus the landmarks transformation, $1/\det(\nabla\Phi)$ plus the deformed grid using BH regularization (middle from left to right), and those using NE regularization (bottom from left to right.)

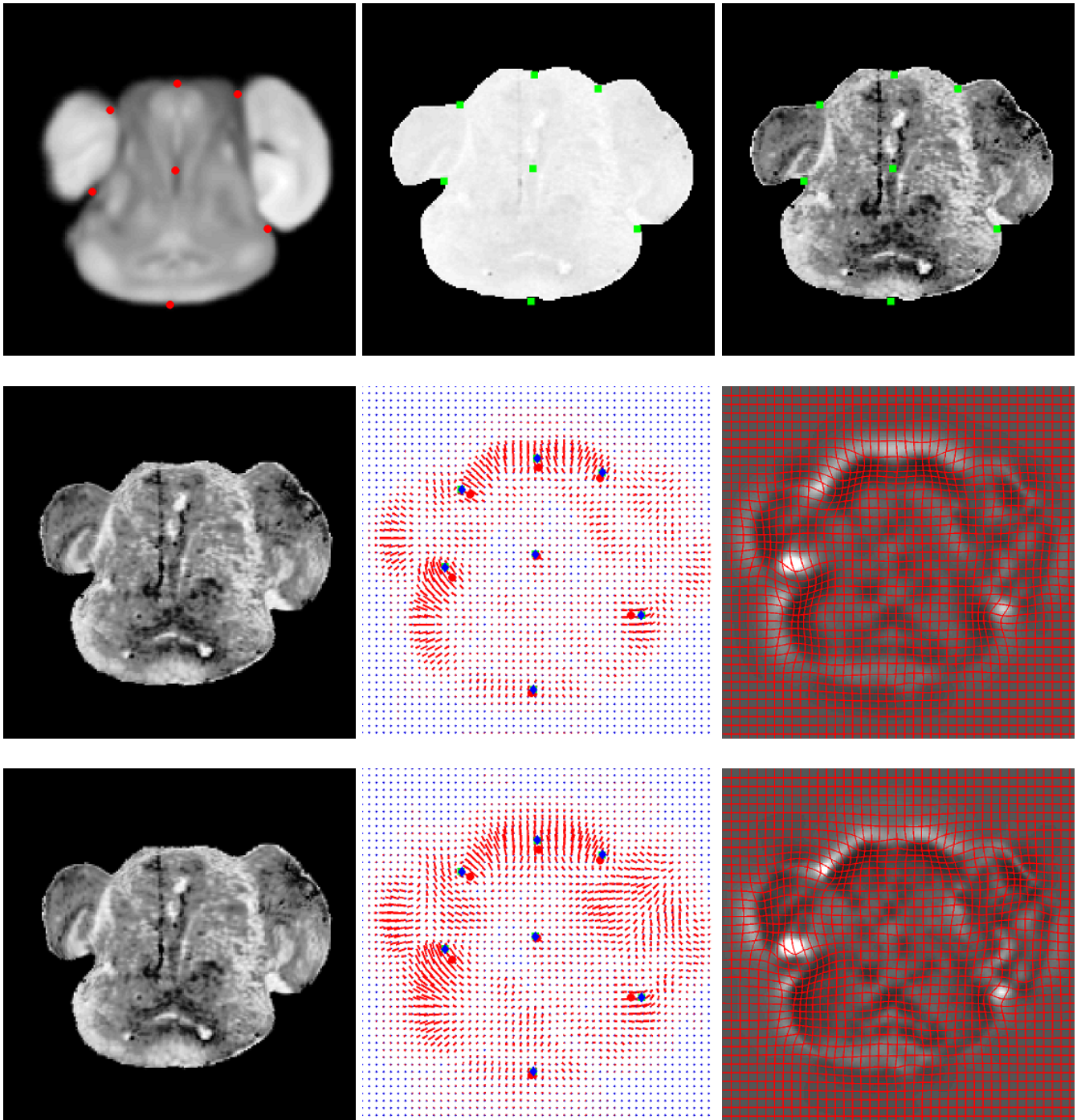


Figure 15: Pair 11: mouse atlas (reference R), gene expression (template T), and gene expression after histogram equalization with specified landmarks (top from left to right); deformed template, deformation field plus the landmarks transformation, $1/\det(\nabla\Phi)$ plus the deformed grid using BH regularization (middle from left to right), and those using NE regularization (bottom from left to right.)

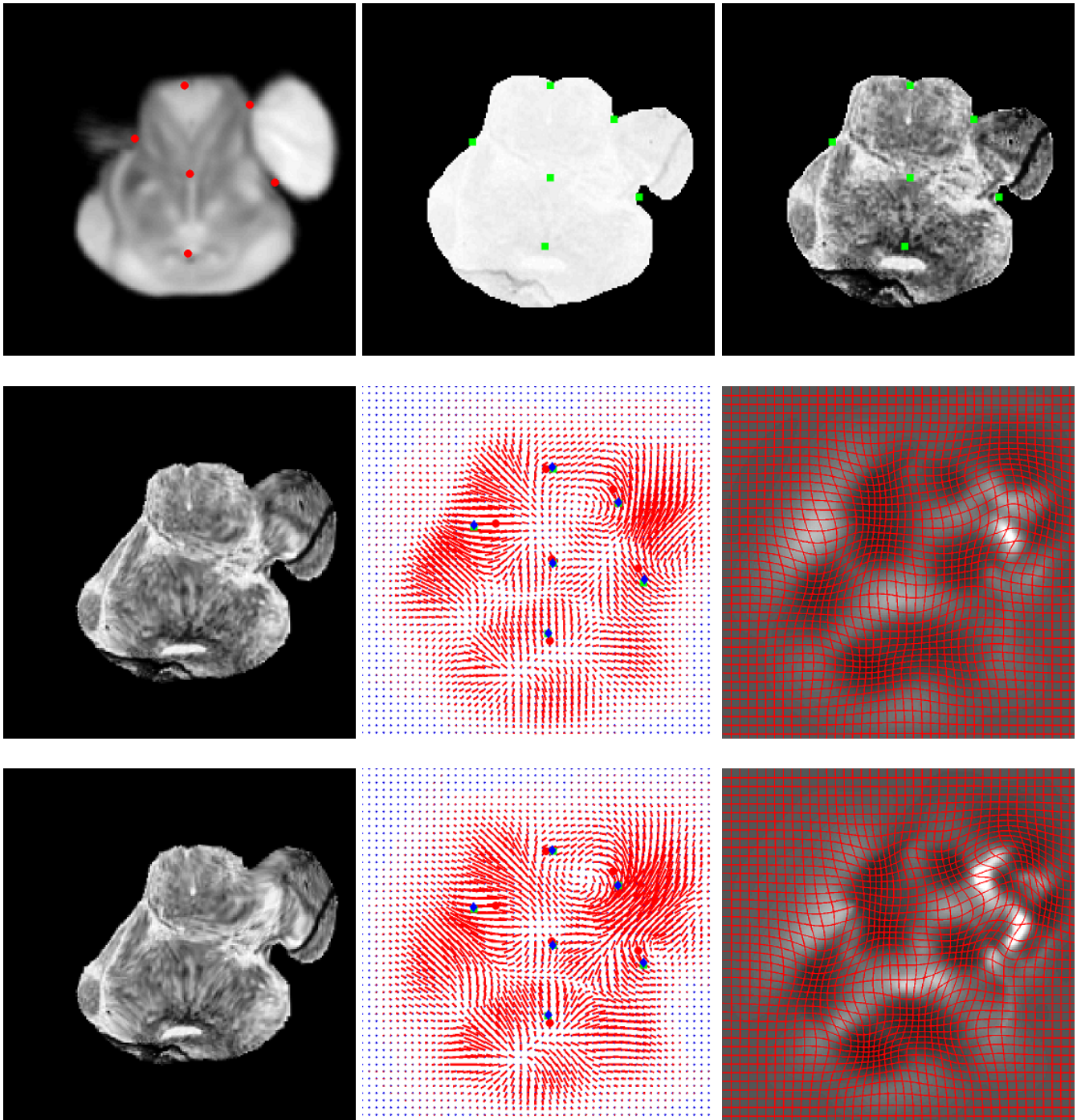


Figure 16: Pair 12: mouse atlas (reference R), gene expression (template T), and gene expression after histogram equalization with specified landmarks (top from left to right); deformed template, deformation field plus the landmarks transformation, $1/\det(\nabla\Phi)$ plus the deformed grid using BH regularization (middle from left to right), and those using NE regularization (bottom from left to right.)

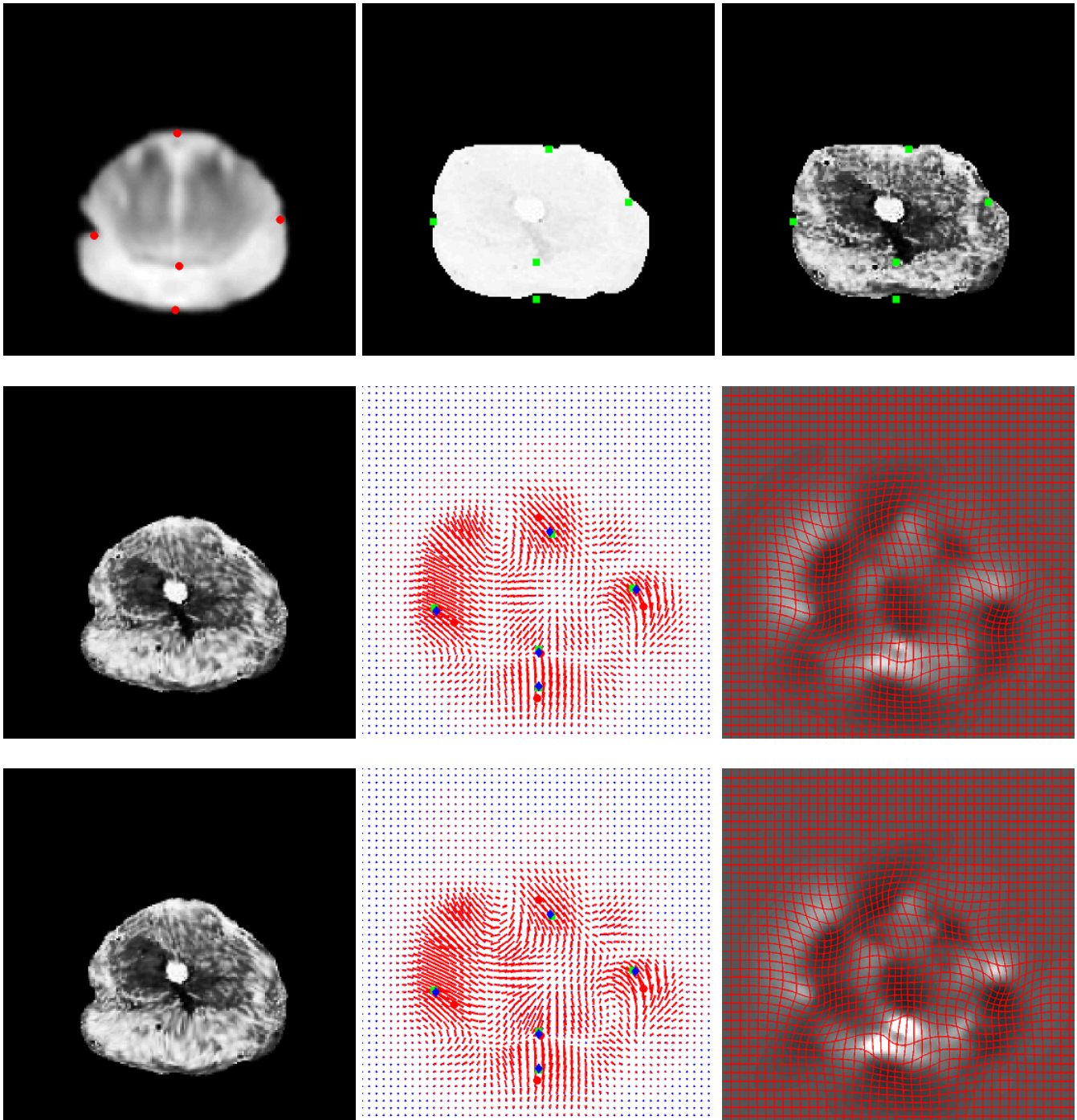


Figure 17: Pair 15: mouse atlas (reference R), gene expression (template T), and gene expression after histogram equalization with specified landmarks (top from left to right); deformed template, deformation field plus the landmarks transformation, $1/\det(\nabla\Phi)$ plus the deformed grid using BH regularization (middle from left to right), and those using NE regularization (bottom from left to right.)

Quantitative Comparisons of the Results Besides the visualization of the registration results shown above, numerics are given in tables. Table 1 and 2 give the landmark distances and the dissimilarity measures after registration by the two models for the eight pairs of images. The nonlinear elasticity model reaches smaller dissimilarities in overall intensity values and in landmark distance.

Table 1: Landmark Distance after Registration

	IMG4	IMG5	IMG6	IMG7	IMG8	IMG11	IMG12	IMG15
LMDist(BH)	0.49519	0.42388	0.26758	0.90027	0.70846	0.11232	0.46912	0.71972
LMDist(NE)	0.49282	0.41299	0.26593	0.74304	0.60741	0.10712	0.34660	0.55106

Table 2: Dissimilarity Measure after Registration

	IMG4	IMG5	IMG6	IMG7	IMG8	IMG11	IMG12	IMG15
$\ T1 - R\ $ (BH)	1,942	1,806	1,168	4,130	3,723	1,255	1,266	3,073
$\ T1 - R\ $ (NE)	1,938	1,790	1,151	4,101	3,693	1,177	1,173	3,058

We also observe that the nonlinear elasticity model has a slightly larger range of values for the determinant of Jacobian in average but also has a higher average percentage of points where the determinant of Jacobian equals to one. Table 3 gives the range of values for the determinant of Jacobian for the eight pairs of images after registration.

Table 3: Range of Values for the Determinant of Jacobian

	IMG4	IMG5	IMG6	IMG7	IMG8	IMG11	IMG12	IMG15
BH	(0.34,3.38)	(0.15,2.11)	(0.28,1.99)	(0.25,2.05)	(0.04,1.87)	(0.23,2.30)	(0.31,2.30)	(0.37,2.12)
NE	(0.32,3.55)	(0.01,3.16)	(0.10,2.15)	(0.08,2.57)	(0.10,2.82)	(0.15,2.40)	(0.18,3.23)	(0.03,2.35)

Table 4 gives the percentage of points where the determinant of Jacobian equals to one after registration by the two models for the eight pairs of images. Now we see that the percentages for both models are very close. The nonlinear elasticity model renders larger percentages for five out of eight image pairs.

Table 4: Percentage of Points where the Determinant of Jacobian Equals to One

	IMG4	IMG5	IMG6	IMG7	IMG8	IMG11	IMG12	IMG15
BH	%52.74	%52.66	%52.73	%51.08	%57.96	%53.35	%59.75	%52.39
NE	%52.73	%52.44	%54.15	%56.39	%52.05	%53.67	%66.52	%54.29

Table 5 gives the iteration numbers by the two models for the eight pairs of images. Number of iterations required by both models are similar given proper choice of parameters; iteration time for the nonlinear elasticity model is about twice as long as that for the biharmonic model (13 to 16 minutes *v.s.* 5 to 7 minutes per 4,000 iterations using Intel(R) Core(TM)2 Duo CPU T7500 @ 2.20GHz processor with code in Matlab); no regridding step is needed for both models for gene data to atlas registration given proper choice of parameters; fewer regridding steps are needed for nonlinear elasticity model for binary images.

Table 5: Iteration Numbers

IMG4	IMG5	IMG6	IMG7	IMG8	IMG11	IMG12	IMG15
10,000	10,000	10,000	200,000	140,000	4,000	80,000	40,000

Table 6 gives the parameters chosen for the two models for the eight pairs of images: the time step $dt = 1$ and the space discretization $h = 1$ for both models. For the biharmonic model, we vary the regularization weighing parameter α and the landmark constraint coefficient γ ; for the nonlinear elasticity model, we vary the coefficient β of the approximation matrix \mathbf{v} and γ while fixing $\alpha = 1$, $\lambda = 1$, and $\mu = 1e - 2$. The choice of α and β does not vary too much among the tested pairs of images; $\alpha \geq 5e + 4$ and $\beta \geq 75e + 3$ will give satisfactory results. The choice of γ more or less depends on the total landmark distance before registration; the larger the landmark distance is, the smaller γ should be. Note that an almost constant (or slightly increasing) ratio, γ/α or γ/β , for each image pair can be found; increasing γ in accordance with α or β by the ratio may result in smoother transformation, faster landmark convergence, but slower similarity convergence.

Table 6: Parameters

	IMG4	IMG5	IMG6	IMG7	IMG8	IMG11	IMG12	IMG15
α	50,000	75,000	50,000	100,000	100,000	75,000	150,000	75,000
$\gamma(\text{BH})$	100,000	700,000	300,000	100,000	100,000	700,000	300,000	150,000
β	100,000	120,000	75,000	100,000	75,000	75,000	150,000	100,000
$\gamma(\text{NE})$	160,000	190,000	300,000	100,000	700,000	700,000	300,000	150,000

Mutual Information Furthermore, we want to evaluate the registration results by comparing how much the deformed template correlates with the reference after being registered by the two models. Such correlation is called mutual information and is formulated as follows:

$$MI_{\mathbf{X},\mathbf{Y}} = \int_{\mathbf{Y}} \int_{\mathbf{X}} p(x,y) \log \frac{p(x,y)}{p(x)p(y)} dx dy,$$

where \mathbf{X} and \mathbf{Y} are random variables; $p(x,y)$ is the joint probability density function of \mathbf{X} and \mathbf{Y} ; $p(x)$ and $p(y)$ are the marginal probability density functions of \mathbf{X} and \mathbf{Y} respectively.

Mutual information quantifies the dependence between \mathbf{X} and \mathbf{Y} , which in our case are the intensity maps of R and T . Considering larger mutual information indicates better regis-

tration, we see in the following plots that the nonlinear elasticity model, indicating by black line, is more desirable in this respect.

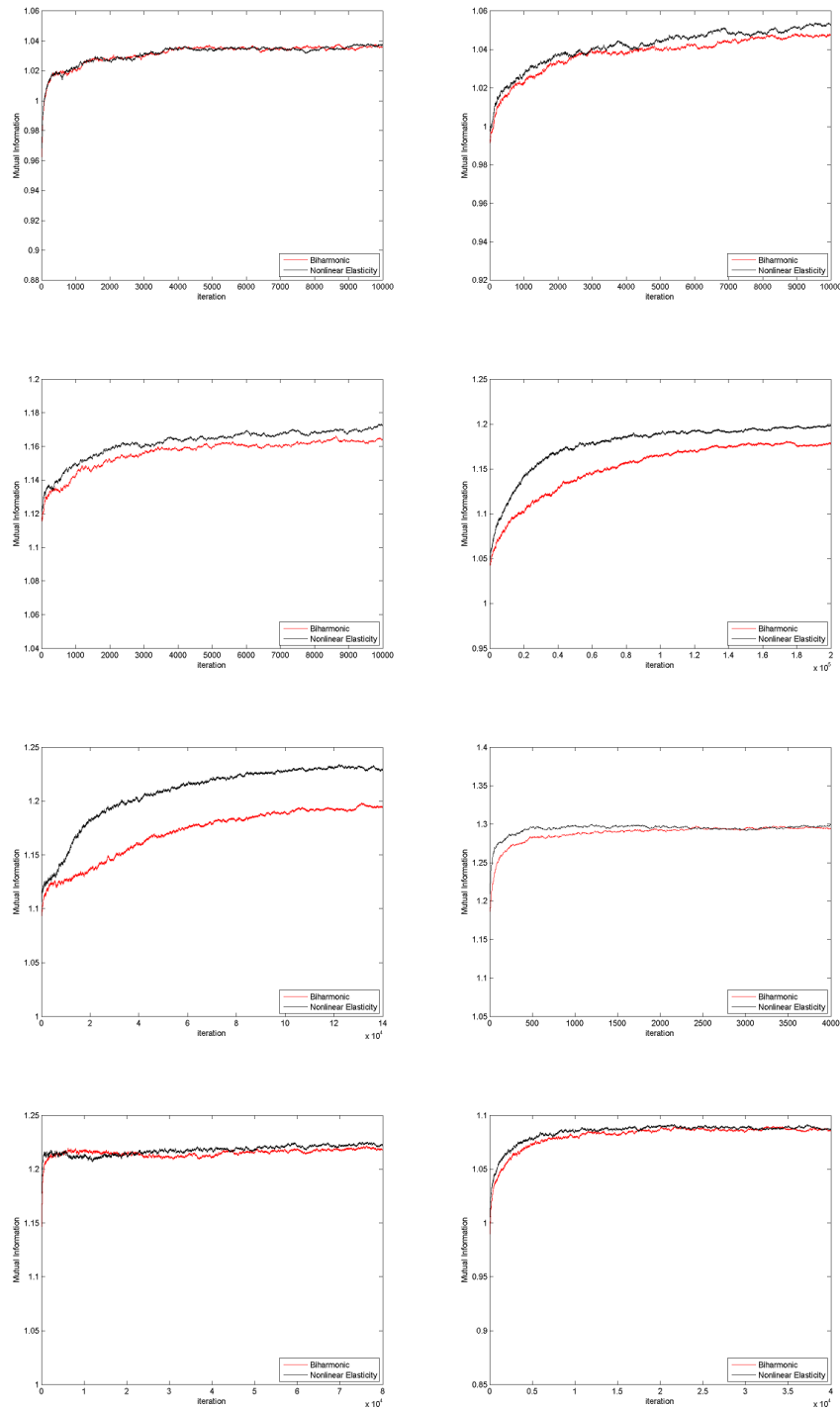


Figure 18: Mutual information increasing with time for all pairs, 4-8, 11, 12, 15, (from left to right, top to bottom) using BH regularization (red line), and NE regularization (black line)

4 Conclusion and future work

We presented variational registration models for obtaining smooth deformations between two dimensional slices of mouse atlas and gene expression data. We proposed a nonlinear elastic regularization with an implementation that removes the nonlinearity in the derivatives and compared it with the biharmonic model. Experimental results showed that the biharmonic model and the nonlinear elasticity model both render large deformation with no regriding step. Moreover, the nonlinear elasticity model renders higher mutual information and better landmark points matching. A better parameter selection and extension to three dimensions will be made.

Acknowledgements We would like to thank Erh-Fang Lee for pre-processing the mouse brain image data and providing us with the landmark points. We also want to thank Igor Yanovsky for his constant examination and helpful suggestions for the numerical implementation of the nonlinear elasticity model. This work was funded by the National Institutes of Health through the NIH Roadmap for Medical Research, Grant U54 RR021813 entitled Center for Computational Biology (CCB).

References

- [1] F. Beg, M. Miller, A. Trouvé, and L. Younes. Computing large deformation metric mappings via geodesic flows of diffeomorphisms. *IJCV*, 61(2):139–157, 2005.
- [2] C. Broit. *Optimal Registration of Deformed Images*. PhD thesis, Computer and Information Science, University of Pennsylvania, 1981.
- [3] G.E. Christensen, M.I. Miller, M.W. Vannier, and U. Grenander. Individualizing neuroanatomic atlases using a massively parallel computer. *IEEE Computer*, 29(1):32–38, 1996.
- [4] G.E. Christensen, R.D. Rabbitt, and M.I. Miller. Deformable templates using large deformation kinematics. *IEEE TIP*, 5(10):1435–1447, 1996.
- [5] P.-G. Ciarlet. *Elasticité Tridimensionnelle*. Masson, 1985.
- [6] M. Droske and M. Rumpf. Imaging science: Morphological image registration and nonlinear elasticity. *SIAM News*, 37(7), September 2004.
- [7] M. Droske and M. Rumpf. A variational approach to non-rigid morphological registration. *SIAM Appl. Math.*, 64(2):668–687, 2004.
- [8] O. Faugeras and G. Hermosillo. Well-posedness of two nonrigid multimodal image registration methods. *SIAM Appl. Maths.*, 64(5):1550–1587, 2004.
- [9] C. Le Guyader and L.A. Vese. A combined segmentation and registration framework with a nonlinear elasticity smoother. *UCLA CAM Report 08-16*, March 2008.
- [10] P.W. Hallinan, G.G. Gordon, A.L. Yuille, P. Giblin, and D. Mumford. *Two- and Three-dimensional Patterns of the Face*. A.K. Peters LTD, 1999.

- [11] H.J. Johnson and G.E. Christensen. Consistent landmark and intensity-based image registration. *IEEE TMI*, 21(5):450–461, 2002.
- [12] E.-F. Lee, R.E. Jacobs, I. Dinov, A. Leow A, and A.W. Toga. Standard atlas space for c57bl/6j neonatal mouse brain. *Anat. Embryol (Berl.)*, 210(4):245–263, 2005.
- [13] T. Lin, E. Lee, I. Dinov, C. Le Guyader, P. Thompson, A. Toga, and L. Vese. A Landmark-Based Nonlinear Elasticity Model for Mouse Atlas Registration. In *Proceedings IEEE ISBI*, pages 788–791, 2008.
- [14] T. Lin, E. Lee, I. Dinov, C. Le Guyader, P. Thompson, A. Toga, and L. Vese. Gene to Mouse Atlas Registration Using a Landmark-Based Nonlinear Elasticity Smoother. In *Proceedings SPIE MI*, volume 7259, pages 72592Q–1–16, 2009.
- [15] A.J. MacKenzie-Graham, E.-F. Lee, I.D. Dinov, H. Yuan, R.E. Jacobs, and A.W. Toga. Multimodal, multidimensional models of mouse brain. *Epilepsia*, 48, Supplement 4:75–81(7), 2007.
- [16] P.V. Negrón Marrero. A numerical method for detecting singular minimizers of multidimensional problems in nonlinear elasticity. *Numerische Mathematik*, 58(1):135–144, 1990.
- [17] M.I. Miller, A. Trounev, and L. Younes. On the metrics and Euler-Lagrange equations of computational anatomy. *Annu. Rev. B. Eng*, 4:375–405, 2002.
- [18] J. Modersitzki. *Numerical Methods for Image Registration*. Oxford University Press, 2004.
- [19] W. Peckar, C. Schnörr, K. Rohr, and H.S. Stiehl. Non-rigid image registration using a parameter-free elastic model. In *BMVC*, 1998.
- [20] W. Peckar, C. Schnörr, K. Rohr, and H.S. Stiehl. Parameter-free elastic deformation approach for 2D and 3D registration using prescribed displacements. *JMIV*, 10(2):143–162, 1999.
- [21] R. D. Rabbitt, J. A. Weiss, G. E. Christensen, and M. I. Miller. Mapping of hyperelastic deformable templates using the finite element method. In *Proceedings SPIE*, volume 2573, pages 252–265, 1995.
- [22] C.O.S. Sorzano, P. Thévenaz, and M. Unser. Elastic registration of biological images using vector-spline regularization. *IEEE T. Biom. Eng.*, 52(4):652–663, 2005.
- [23] Hemant D. Tagare, David Groisser, and Oskar Skrinjar. A geometric theory of symmetric registration. In *Proceedings of CVPRW’06 IEEE*, 2006.
- [24] R.M. Temam and A.M. Miranville. *Mathematical Modeling in Continuum Mechanics*. Cambridge, 2005.
- [25] I. Yanovsky, P. Thompson S. Osher, and A. Leow. Topology preserving log-unbiased nonlinear image registration: Theory and implementation. *CVPR*, pages 1–8, 2007.
- [26] I. Yanovsky, S. Osher, P. Thompson, and A. Leow. Log-unbiased large-deformation image registration. *VISAPP*, 1:272–279, 2007.